The 2019-2020 Indios, Puerto Rico earthquake sequence: seismicity and faulting

Blaž Vičič[1], Seyyedmaalek Momeni[1,2], Alessandra Borghi[1,3], Anthony Lomax[4], Abdelkrim Aoudia[1]

[1]The Abdus Salam International Centre for Theoretical Physics, I-34151 Trieste, Italy
[2] Ecole Polytechnique Fédérale de Lausanne, Geo-Energy Laboratory, Lausanne, Switzerland
[3] Istituto Nazionale Geofisica e Vulcanologia, sezione di Bologna, Italy
[4]ALomax Scientific, Mouans-Sartoux, France

Abstract

The 2019-2020 Indios, Puerto Rico earthquake sequence ruptured on multiple faults with several moderate magnitude earthquakes. Here we investigate the seismotectonics of this fault system using high precision hypocenter relocation and inversion of the near-field strong motions of five largest events in the sequence ($5.6 \leq Mw \leq 6.4$) for kinematic rupture models. The Mw6.4 mainshock occurred on an NE striking, SE dipping normal fault. The rupture nucleated offshore ~15 km SE of Indios at the depth of 8.6 km and extended SW-NE and up-dip with an average speed of 1.55 km/s, reaching the seafloor and shoreline after about 8 seconds. The Mw5.7 and Mw5.8 events on 6th and 7th January 2020, respectively, occurred on two E-SE striking, near-vertical, left-lateral strike-slip faults. However, the 7th January 2020 Mw5.8 aftershock which occurred only 10 minutes after the mainshock, ruptured on a fault with almost the same strike as the mainshock but situated ~8 km further E, forming a set of parallel faults in the fault system. On 11th January 2020, a Mw6.0 earthquake occurred on a N-NE striking, W dipping fault, orthogonal to the faults hosting the strike-slip earthquakes. We also apply template matching for the detection of missed, small magnitude earthquakes and to study the spatial evolution of the main part of the sequence. These detections show multiple examples of acceleration phases before moderate earthquakes and reveal migration patterns within the sequence. Using the template matching results along with GPS analysis, we image the temporal evolution of a foreshock sequence (Caja swarm). We propose that the swarm and the main sequence were a response to an inferred tectonic transient that most likely originated on the Muertos subduction as a slow-slip event.

1. Introduction

The 2019-2020 Indios, Puerto Rico earthquake sequence included multiple moderate earthquakes (Mw>5.0) that ruptured different faults with different faulting mechanisms (University of Puerto Rico, 1986). The swarm-like Indios sequence started in July 2019 with a smaller offshore Caja swarm, 14 km south of Ponce, Puerto Rico. The activity continued with the main sequence starting on December 28th, 2019 comprising more than 10 Mw>=5.0 earthquakes and the largest, Mw6.4, normal faulting earthquake on January 7th 2020.

The island of Puerto Rico (Fig. 1) is located in a zone of convergence between the North American (NAP) and Caribbean (CP) tectonic plates (Huérfano et al., 1994). North of the island, the NAP is subducting obliquely beneath the CP at the rate of (20 ± 0.4) mm/yr (DeMets et al., 2010) along the east-west striking Puerto Rico trench. Oblique subduction results in strain partitioning and favours microplate tectonics along the eastern Great Antilles island arc (Jansma et al., 2005). The Puerto Rico microplate (PRm) is part of the CP and is moving ENE relative to NAP (Jansma et al., 2000). On the southern margin of the PRm, the CP is subducting under the Greater Antilles crust (van Benthem et al., 2013). Slip rates derived from GPS velocities estimate convergence between 3mm/yr south of Hispaniola island and 0.2mm/yr south of Puerto Rico (Benford et al., 2012, Bruna et al., 2010).

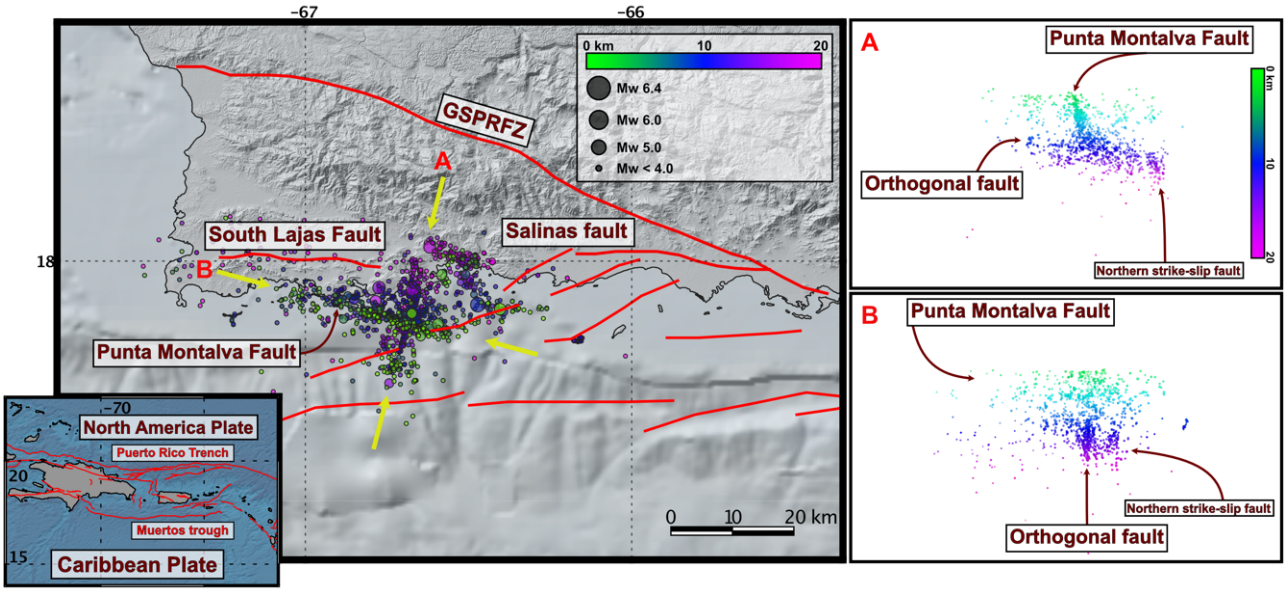

Figure 1: The 2019-2020 Indios, Puerto Rico earthquake sequence colored by depth .The red lines represent known faults. Offshore faults are from Bruna et al. (2015).The inset figure shows generalized tectonic regime. Figures A and B correspond to the NNE-SSW and ESE-WNW profiles respectfully.

Rare moderate size earthquakes occurred in and near Puerto Rico in the 20th century and earlier (Reid et al., 1919, Doser et al., 2005). The majority of instrumental earthquakes (Mw>=3.0) is located north of the island, along the NAP subduction zone. Seismically most active are the SW and SE regions of Puerto Rico (Huérfano et al., 2005). The shallow seismicity of southern Puerto Rico is related to the internal deformation within the Puerto Rico fault zone in the NW-SE direction, while the intermediate depth seismicity occurs above a north dipping zone beneath the island (Huérfano et al., 2005). The tectonics of the southern part of the island is partially controlled by E-W oriented strike-slip faults; South Lajas, Punta Montalva and Salinas faults, which form a more than 80km long fault system. Recent paleoseismologic studies showed that some of the strike-slip faults in the SW of Puerto Rico ruptured in the last 10.000 years and pose a considerable seismic hazard. The South Lajas fault experienced two surface

rupturing events, around 5.000 years ago (Prentice and Mann, 2005), while the Salinas fault ruptured twice in the past 10.400 years (Piety et al., 2018).

We study the geometry (Fig. 1) of the faults activated in the SW of Puerto Rico during the 2019-2020 Indios sequence by relocating the sequence and performing the kinematic source-rupture modelling of the five largest events ($5.6<Mw<6.4$). The relocated events and kinematic rupture inversion reveal a sequence that activated a parallel set of WNW-ESE striking strike-slip faults, connected by an orthogonal, NNE-SSW strike-slip fault and oblique, NE-SW striking normal faults. We adopt the matched filter event detection approach to study the temporal and spatial evolution along the faults and in combination with GPS data analysis. We suggest that the sequence was preceded by a transient deformation that most likely loaded the system.

2. Methods

We obtained an earthquake catalog for the Puerto Rico area (latitude 17.56º to 18.73º, longitude -65.50º to -67.80º) from 2019-01-01 to 2020-05-02, M≥2.0 through earthquake.usgs.gov (Benz, 2017) including corresponding PRSN and USGS P and S arrival times, time uncertainties and first-motions. This catalog contains about 7,000 events. We obtained from IRIS-DMC metadata for permanent and temporary stations used for relocation (within 1º of latitude 38.16º, longitude -117.88º; near the M_w6.5 epicenter) and waveforms for coherence analysis, matched-filter and kinematic source analysis.
For the geodetic analysis we use the IGS14 continuous GPS (cGPS) position time-series of the Puerto Rico Island stations provided by the repository of the Nevada Geodetic Laboratory (Blewitt et al, 2018).

2.1. Precise, absolute earthquake locations

We obtained absolute relocations for the study area using source-specific, station travel-time corrections (SSST; Richards-Dinger & Shearer, 2000) and high-precision relocation based on waveform coherency between events. This approach produces enhanced relative location and clustering of events, and allows analysis of model- and data-dependent error in the hypocenters (Lomax, 2020). We performed absolute earthquake location with the NonLinLoc algorithm (Lomax et al., 2000, 2014; NLL hereafter), which uses efficient global sampling algorithms to obtain an estimate of the posterior probability density function (PDF) in 3D space for absolute hypocenter location. The location PDF provides a complete description of likely hypocentral locations, includes comprehensive uncertainty information, and allows robust application of waveform coherency relocation. Within NLL, we used the equal differential-time (EDT) likelihood function (Font et al., 2004; A. Lomax, 2005, 2008; Lomax et al., 2014; Zhou, 1994), which is very robust in the presence of outlier data caused by large error in the arrival-times or predicted travel-times. We performed all locations using a search range in depth from 1 to 60 km depth. The shallow limit is a prior constraint required to suppress unreasonably shallow, maximum likelihood depths for numerous events which exhibit double PDF solutions in depth. We used a smoothed, minimum 1D P wave velocity model (Fig. A1) or Puerto Rico and the U.S. Virgin Islands (Huérfano et al., 2010) to seed NLL SSST relocation. We used a finite-differences, eikonal-equation algorithm (Podvin & Lecomte, 1991) to calculate travel-times for P phases for each station, and obtained S phase travel times from these P times through Vp/Vs=1.71.

We relocated events in the Puerto Rico catalog in two stages. First, starting with the initial NLL locations without station corrections, we iteratively generated SSST corrections which vary smoothly within a 3D volume to provide a source-position dependent correction for each station and phase type. We used smoothing distances of 32, 16, 8 and 4 km. Only P and S arrivals with residuals of ≤2.0 sec for relocated events meeting minimum quality criteria are used for update at each iteration. See supplementary material Methods A1 for more details. We relocated the full catalog using the 5 km smoothing-length, SSST corrections (Fig. A2a). In the second relocation stage we greatly reduced absolute location error by combining location information across events based on waveform coherency between the events. This absolute coherency relocation is based on the concept that if the waveforms at a station for two or more events are very similar (have high coherency) up to a given frequency, then the distance separating these "multiplet" events is small relative to the seismic wavelength at that frequency and the events represent stress release on the same, small fault patch (Geller & Mueller, 1980; Poupinet et al., 1982, 1984).

The NLL coherence relocation for a target event is a stack over 3D space of the event's SSST location PDF and the SSST PDF's for other events, each weighted by the waveform coherency between the target event and the other event. Unlike differential-time based relative location, absolute coherency relocation requires waveforms from as few as one station, allowing precise relocation for sparse networks, and for foreshocks and early aftershocks of a mainshock sequence or swarm before temporary stations are installed. See the Supplementary material Methods A2 for more details.

The final coherence locations are shown in Fig. A2b. The median formal errors (e.g. with velocity model fixed and assuming only Gaussian, aleatoric error) for the NLL, NLL-SSST and final, NLL-SSST-coherence locations in both models are listed in Table 1.

2.2. Matched-filter

We used a matched-filter detection algorithm (Gibbons & Ringdal, 2006; Shelly et al., 2007, Vuan, et al. 2018) to improve the magnitude of completeness of the initial catalog and study possible spatio-temporal patterns of the sequence (Vičič et al. 2019).
We used waveform data from the 18 closest available stations of the PR seismic network from the beginning of 2019 until the end of January 2020. The waveform data were filtered between 2 and 8 Hz, where the peak energy of most events is expected and their signal to noise ratio is highest, and downsampled to 20 Hz to speed up processing.
We prepared a template catalogue of all initial catalog events with semi-major axis <= 5km for the detection of additional, similar earthquakes. The templates were cut from 2.5s before to 2.5s after manually picked S phase arrival times on all available channels and stations. We visually inspected all the templates and removed those of low quality or those that had problems with missing or bad data.
To detect new events, the templates were correlated with the continuous waveform data. The sliding-window cross-correlation function (CCF) for each template was calculated with 1 sample step. CCFs were calculated for each station and channel for individual templates and then stacked to form a mean daily CCF trace. For a positive detection we set a threshold of 12*median absolute deviation of the daily trace. After a successful scan of the data we only selected events with inter-event times larger than 3s in order to not include the same event multiple times due to detections from multiple templates. The candidate for detection inside this time window was that with the highest threshold value. The magnitude of the detected event was calculated as the median value of the maximum amplitude ratios for all channels between the template and detected event with a 10-fold increase in amplitude corresponding to a one-unit increase in magnitude (Peng, et al. 2009).

2.3. Kinematic source inversion

The Indios sequence included five moderate 5.6<Mw<6.4 events (Fig. A3, Table A1; hereinafter EV#1-EV#5).
For kinematic source inversion we used near-field strong motion displacement time series derived from digital three-component accelerograms of the PRSN network (Fig. A3). The displacement data were rotated to a defined cartesian coordinate system and filtered with an a-causal, fourth-order Butterworth filter in the frequency ranges between 0.03 – 0.4 Hz. The selected frequencies depend on the quality of data and the used 1-D velocity model of area.
The elliptical sub-fault approximation method (Di Carli et al., 2010; Twardzik et al., 2012; Ruiz & Madariaga, 2013; Momeni et al., 2019; Vičič et al., 2020) is used to retrieve the robust features of the ruptures. This method estimates a rupture in a small number of elliptical patches

(usually up to three). Nine parameters are enough to define each slip patch: five to define the ellipse geometry and four for slip, rupture speed, rake, and rise time.
The inversion process consists of sampling the trial rupture models by the neighborhood algorithm (Sambridge, 1999a, b) in widely defined ranges for the parameters. Trial synthetic displacement wavefields at each station were computed with Axitra code (Cotton and Coutant, 1997). The synthetic wavefields were compared to observations using the Spudich & Miller (1990) cost function which defines a waveform fit in percent. After sufficient iterations of sampling trial models by the adopted algorithm (usually up to 700), we reached convergence to the final model. More details on the inversion procedure are given in Momeni et al., (2019). We used the hypocenters obtained in section 2.1 as initiation points of ruptures (Table 1). Considering the possible errors in hypocenter location and origin time, we allowed the hypocenters to shift ±1 km along both strike and dip on the fault plane. First, we searched among the nodal planes of the GCMT reported focal mechanism (see Data and Resources) for the geometry of each rupture that provides a rupture model with best waveform-fit to the observations. Selected rupture geometry for all the events are provided in Table 1.

Table 1. Rupture inversion information and results for the five largest earthquakes of the 2020 Puerto-Rico seismic sequence.

Event #	Date yyyy/mm/dd	Time hh:mm:ss	Lat. (°)	Long. (°)	Mag. (Mw)	Depth (km)	Strike (°)	Dip (°)	Freq (min-max) Hz	M0 (Nm)
1	2020/01/06	10:32:23	17.8991	-66.8092	5.7	4.5	284	59	0.05-0.2	5.7 E+17
2	2020/01/07	08:24:31	17.9311	-66.7904	6.4	8.6	44	58	0.03-0.4	5.6 E+18
3	2020/01/07	08:34: 5.8	17.9337	-66.736	5.6	6.84	45	52	0.06-0.2	2.7 E+17
4	2020/01/07	11:18:46.7	18.009476	-66.7681	5.8	13.25	296	69	0.05-0.3	6.3 E+17
5	2020/01/11	12:54:49.5	17.8942	-66.849	6.0	18.72	195	67	0.05-0.3	1.4 E+18

After selection of geometry for each event, we ran 10 independent inversions each having slightly different model parameters space. With this we investigate different possible rupture models that can provide the same waveform-fit to the observations. The 10 final rupture models for each event are reported in the Supplementary Material A3 and the preferred rupture models for these events are chosen based on closeness of their scalar seismic moments to the GCMT and USGS point source inversion results (Fig. 2).

2.4. GPS

We analysed the position time-series (see Data and Resources) following the procedure described in Barzaghi & Borghi, (2018). By considering the temporal correlation among the data and using the least-square estimation method we determined the linear trends (tectonic velocity), seasonal signals, discontinuities due to the station equipment and reference frame changes or seismic events. In Fig. 4a we report the estimated velocity vectors of the cGPS stations for the planimetric components and the velocities with respect to the NAP. Vertical velocities are mostly positive and are reported in Fig A10. The strain-rate principal axes shows a NS stretching especially across the Great Southern Puerto Rico Fault Zone (GSPRFZ, Piety *et al.* 2018) (Fig. 4c). All of the cGPS stations are characterized by spatial correlation signals, also known as the common mode error (CME). CME can be reduced using different approaches such as the stacking technique (Wdowinski et al., 1997), Principal Component Analysis (PCA), Karhunen-Loeve expansion (KLE) (Dong et al., 2006) and Independent Component Analysis (ICA) (Liu et al., 2015) that represents a Blind Source Separation (BSS) method. These

methods, especially PCA and ICA are also used for transient detection as in (Ji & Herring 2013, Borghi *et al.* 2016, Gualandi *et al.* 2016, Vičič et al, 2020). Careful investigation is required to discriminate CME and transients in the cGPS time series.

For some cGPS stations, data are available from 2006, while others started to operate as late as 2017 (Table A6). We focused our investigation in the period from 10th of September 2019 to 27th December 2019 because it represents a continuous time range with small data gaps and was characterized by increasing seismicity rate. To increase the signal-to-noise ratio of the data and fill the small gaps, the residual time-series were temporally filtered testing two independent methods: the least-square collocation method (LCS) (Borghi et al. 2009; Borghi et al. 2016) using the covariance functions obtained by the analysis of the temporal correlation, and the moving average method (MA) with data windows of two weeks. As described in the supplementary material the two filtering methods provided analogous results (Fig. A11). PCA and BSS methods, like FastICA and variational Bayesian Component Analysis (vbICA) were applied on the residual time-series for transient signals research and will be discussed in the following chapter.

3. Results

3.1. Geometry of the activated fault system

The kinematic source inversion of the five largest (5.6<Mw<6.4) earthquakes (Fig. 2, Figs. A4-9) and precisely located fore- and aftershocks show that at least five faults were activated. The two dominant parallel faults with WNW-ESE direction ruptured with strike-slip events (EV#1 and EV#4). Southern fault aligns with geologically mapped Punta Montalva fault (Roig-Silva et al., 2013), while the location of the northern fault is less well resolved but lies in an area between two active strike-slip faults – South Lajas fault (Prentice et al., 2005) and Salinas fault (Piety et al., 2018). Depth distribution of seismicity along Punta Montalva fault during this sequence is shallower than 10km and extends for 30km in WNW-ESE direction. Whether or not the Caja swarm lies on the continuation of Punta Montalva fault is difficult to evaluate. If this is the case, a 20km seismic gap exists between the swarm and the activated segment of the fault that ruptured. Depth distribution of seismicity on the northern strike-slip fault is deeper, compared to the Punta Montalva fault, with events between 12 and 22km. The length is around 12km in the WNW-ESE direction.

Bounded between two strike-slip faults, two NE-SW striking normal faults (in agreement with the initial InSAR results (López et al., 2020) ruptured with the Mw6.4 (EV#2) mainshock and the Mw5.6 aftershock (EV#3) that occurred on a fault located 6km E of the mainshock. They do not align with any previously known normal faults (Bruna et al., 2015).

Finally, EV#5 earthquake ruptured a 22km long, NNE-SSW orthogonal strike-slip fault with a unique geometry (discussed in the Results). Northwards it is bounded by the north strike-slip fault while towards south it crosses Punta Montalva fault. The deepest aftershocks are towards the north while the shallowest ones are towards the south.

EV#1 nucleated at the depth of 4.5±1km. The rupture evolved mostly toward up-dip and slightly to the W with an average rupture velocity of 1.8km/s (Vs = 3.1) for ~2.6s. It released a total scalar seismic moment of 5.7E17Nm which is comparable to the GCMT and larger than USGS results (4.5E17Nm and 3.16E17Nm, respectively). The rake is well resolved (-21°) showing a left-lateral strike-slip mechanism. A maximum slip of 1.8m is observable at the depths of 3 to 4km, between 0.7s and 1.7s after the nucleation.

EV#2 nucleated at the depth of 8.6km. The rupture evolved on an NE striking (44 °) SE dipping (58°) fault plane with an average speed of 1.55km/s. It reached the surface ~8s after the nucleation (Fig. A6b). The rupture occurred in 10s and released a total scalar seismic moment of 5.6E18Nm, close to the GCMT and USGS results (4.72E+18Nm and 5.04E+17Nm, respectively). It showed a reasonable waveform fit of 75%. Average rake was -124° revealing a normal faulting mechanism with a right-lateral strike-slip component.

EV#3 rupture started at the depth of 6.8km. The slip evolved toward shallow depths and slightly to the NE on a NE striking (45°) SE dipping (52°) fault. The whole rupture occurred in 3.3s and released a total scalar seismic moment of 2.74E17Nm. The waveform fit was still reasonable (82%) (Fig. A7c).

EV#4 nucleated at a depth of 13km. Its slip evolved mostly down-dip and towards E on an ~E striking, N dipping fault plane with a rupture velocity 2.5km/s, lasting 2.4s with a scalar seismic moment of 6.3E17Nm, larger than the GCMT and USGS results (5.5E17Nm and 3.63E17Nm, respectively). This model has an 84% waveform fit. The rake is 11°, showing almost pure left-lateral strike-slip mechanism.

On the 11th January, EV#5 nucleated at the depth of 19km. Its rupture evolved up-dip and mostly to the N on a ~N-S striking (195°), West dipping (67°) fault plane with an average speed of ~2.8km/s that lasts for ~3.5s. It released a total scalar seismic moment of 1.4E18Nm. This

model has a waveform fit of 89%. The obtained rake was -153° showing a right-lateral strike-slip mechanism with a rise time of ~1.6s.

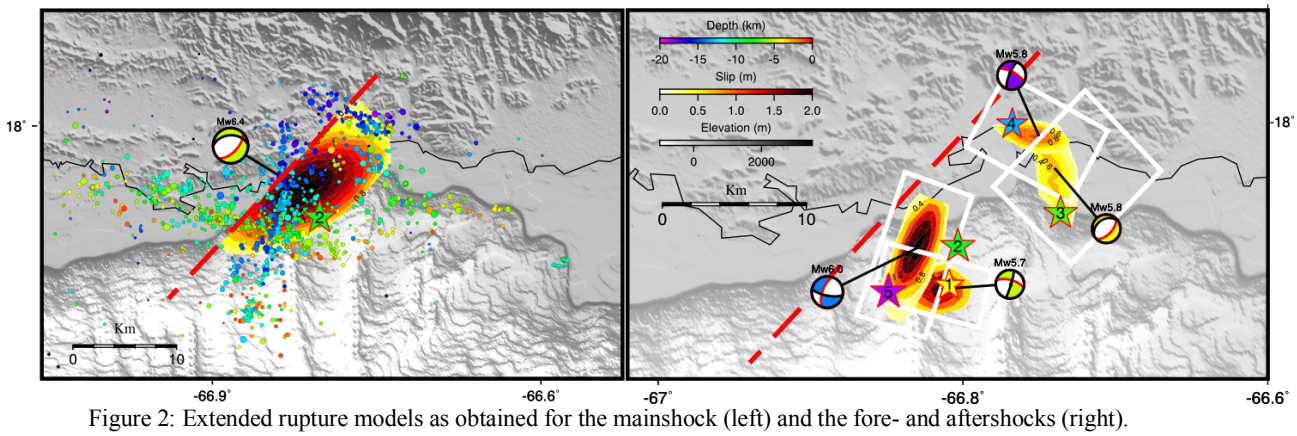

Figure 2: Extended rupture models as obtained for the mainshock (left) and the fore- and aftershocks (right).

3.2. Temporal and spatial evolution

Using well located earthquakes as templates we were able to detect additional events, which gave a better understanding of the sequence development.

The sequence began as a low magnitude (M<3.5) swarm, 14km south of Ponce, Puerto Rico in July 2019, ending in January 2020. The newly detected earthquakes in this swarm were temporally split into 3 clusters (Fig. A13) with the most and largest earthquakes in the third cluster.

The main sequence initiated along the Punta Montalva fault (Fig. 3a, b). Prior to the sequence, detected seismicity along the fault was spread over time and we were unable to detect more events than reported in the original catalog.

The sequence started on the 28th December 2019 with a Mw4.7 earthquake, followed a few hours later by a Mw5.0 earthquake and its aftershock sequence. After the Mw5.0 the aftershocks slowly extended both in WNW and ESE direction (Fig. 3a) with the migration velocity towards WNW slightly higher than towards ESE. The WNW side of the Punta Montalva fault was more productive in terms of aftershock than its ESE extent. The ESE migration continued until the 6th of January 2020 when the largest, Mw5.8 earthquake took place in the ESE portion of the Punta Montalva fault. The Mw5.8 earthquake was preceded by a foreshock sequence of its own in a 2 km wide area of elevated seismicity less than 1 km away from its hypocentre (Fig. A17). In the aftermath of the Punta Montalva fault earthquake, the aftershocks were distributed all along the previously activated fault segment. Few hours after the Punta Montalva fault earthquake an aftershock with Mw4.9 happened at the most ESE part of the Punta Montalva fault. The Mw4.9 earthquake was preceded by an acceleration phase (Fig. A18) at the edge of the activated Punta Montalva fault that stopped with the earthquake. The migration with unchanged velocity continued towards ESE until 13th of January 2020 when an acceleration phase (Fig. A19) started in the vicinity of a Mw5.2 earthquake that ruptured the most ESE segment of the reactivated part of Punta Montalva fault.

On 7th of January 2020 the Mw6.4 mainshock of the sequence occurred on a normal fault between the Punta Montalva fault and the northern strike-slip fault (Fig. 3b). It was followed by a Mw5.8 normal faulting earthquake NE of its hypocentre. Following the Mw5.8 event, a Mw5.7 strike-slip earthquake ruptured the northern strike-slip fault. The aftershocks along the normal fault were confined towards the north with the area where the fault intersects with the northern strike-slip fault and towards the south, with an intersection with Punta Montalva fault. The aftershock sequence on the normal fault was less energetic than on the northern strike slip

fault but this changed on the 8th January, 2020, when a Mw4.7 earthquake took place on it (Fig. 3b)

On 11th January, an orthogonal fault (Fig. 3b) was activated with a Mw6.0 left-lateral strike slip earthquake. Towards the N, aftershocks were confined by the northern strike slip fault, while towards the S, aftershocks extended past the Punta Montalva fault.

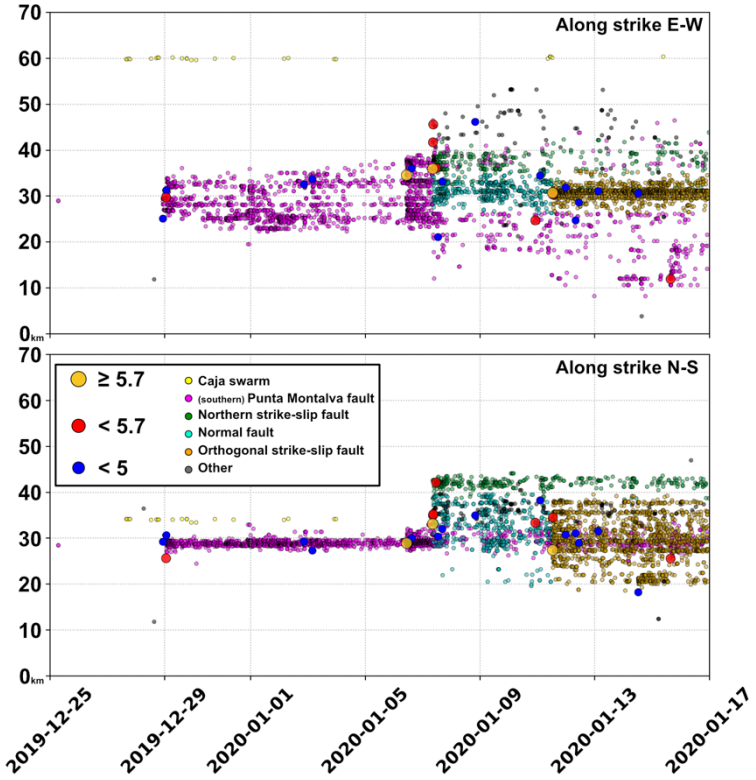

Figure 3: Top figure shows seismicity evolution along the strike of strike-slip faults, highlighting the features of Punta Montalva fault and northern strike slip fault. Bottom figure shows seismicity evolution along the strike of orthogonal strike-slip fault, highlighting the evolution of seismicity on the normal fault that ruptured with the Mw6.4 mainshock and along the orthogonal strike slip fault.

3.3. Geodetic transients

The PCA method applied on the filtered residuals showed that the most important contribution was described by the first two principal components that describe around 80% of the variance. The northern and vertical components are characterized by a discontinuity between October and November 2019, confirmed by Bayesian inference test (Borghi et al., 2012, 2016) on the 21st of October, 2019 (day of the year 294 ± 2) with a total probability of 99%. A posterior probability related to the Bayesian estimation of the discontinuity is presented in Figure A12 where we observe the effect of the filtering method used for the detection of discontinuity epoch. PCA and vbICA show very similar behavior in the first principal (PC1) and independent components (IC1) (Fig. A13) and confirm the individuation of a discontinuity in the northern and vertical components. The eastern component does not show a sharp discontinuity (Fig. A4) but rather a positive linear trend that is correlated with the cumulative number of earthquakes in September 2019 (Fig. A14). PC1 could be interpreted as CME signal that should be removed from the time-series, however some considerations suggest that the PCs and ICs reported in Figure A13 represent a geophysical signal present all over Puerto Rico Island in October 2019. Since all the cGPS contribute to the first components (Fig. A13, A15) we suppose that this corresponds to the complex tectonic signal. Moreover, the observed discontinuity temporally

falls in the third seismic cluster of Caja swarm, characterized by the most and largest earthquakes (Fig. A14) as already mentioned in Chapter 3.2.

Due to the discontinuity corresponding to the period of increasing seismicity, we analysed this period and computed the displacement field related to this event for each station by least square estimation. The displacement field vectors point towards the south (Fig. 4b) while at the same time, stations undergo uplift (Fig. A16). We also note that the principal axes of the 2d strain tensor are not aligned to the principal axes of the strain-rate tensors due to the tectonic velocity of the stations, but rather represent a divergence behaviour in the NE-SW direction (Fig. 4c)

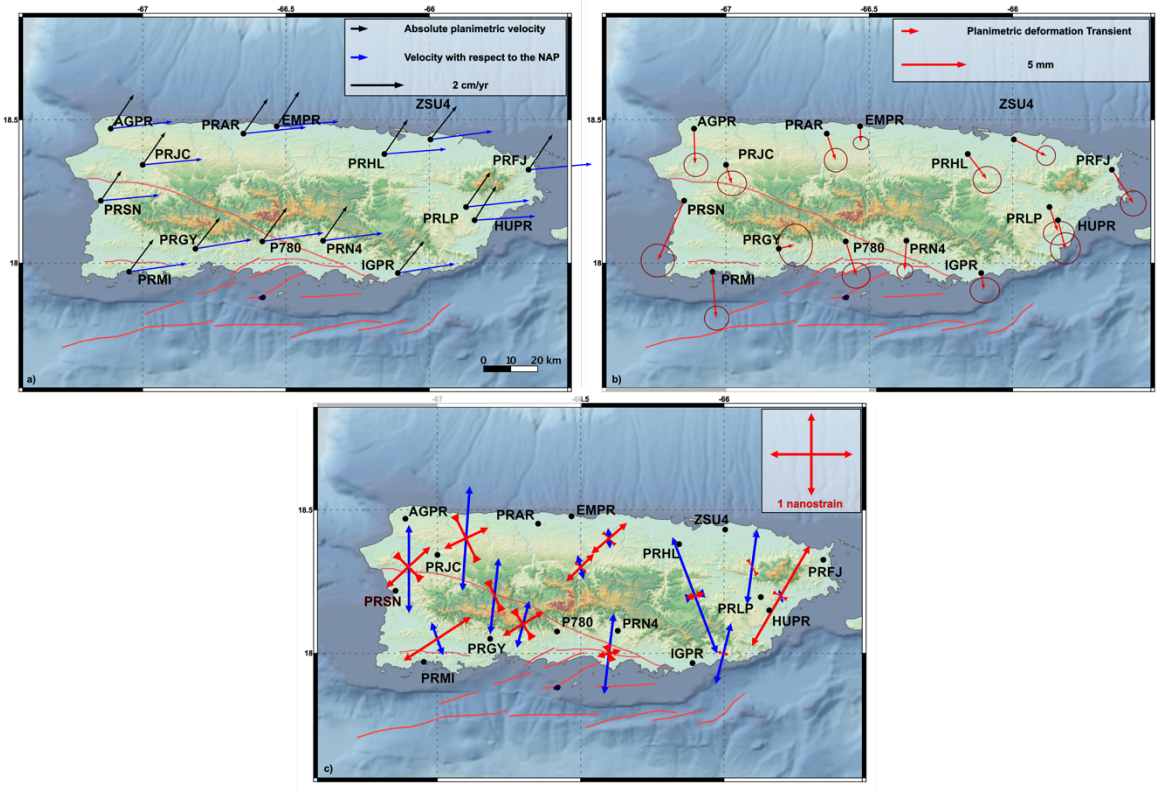

Figure 4: a) Absolute planimetric velocities (black arrows) and velocities with respect to the NAP (blue arrows). b) Estimate of the planimetric deformation due to the SSE signal pointed out by the BSS at time 21st October 2019. c) The blue arrows represent the planar strain-rate values obtained by the estimated velocity, whereas the red arrows are the principal axis of the strain tensor due to the SSE recorded on 21st October, 2019. The red lines are the faults.

4. Discussion

The geometry defined by the relocated events and inversion of the well recorded Mw5.6+ earthquakes on strike-slip and normal faults highlights a very complex system of faulting. We observe that the northern and Punta Montalva faults form a system of parallel strike-slip faults while the normal fault, that hosted the mainshock of the series, forms an oblique structure between them. Additionally, the two parallel strike slip faults are connected by an orthogonal fault deepening from south northward. Its northern edge is bounded by the northern strike-slip fault, while towards the south, it continues past the Punta Montalva fault.

These observations show that the geometry of faulting within this sequence is controlled by a larger structural feature – the subduction of CP underneath Puerto Rico as presented in Figure 5. Due to oblique subduction of CP, the area is characterized by strain partitioning with strike slip faults as Punta Montalva northward of the subduction. Strain partitioning is possible if the coupling between subducting and overriding plate is high (Haynie et al., 2017).

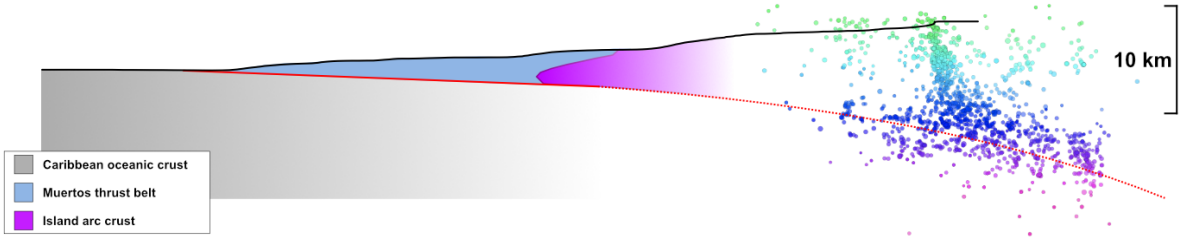

Figure 5: A south-north profile over the SW part of the Puerto Rico Island. The full red line represents the subduction interface (Bruna et. al, 2015), while the dotted red line represents inferred subduction dipping towards the north.

The seismicity on the orthogonal fault follows the subducting CP interface and is most likely constrained by differences between the overriding crust and the CP slab, such as a transition from velocity weakening in the crust where brittle deformation is promoted to a velocity strengthening regime in the slab that does not allow slip propagation.

The discontinuity, observed with PCA analysis of the cGPS time series, shows that the October 21st 2019 transient is common to every station of the Island. This, and the fact, that the cGPS stations show almost 90º (Fig. 4a, b) change of velocities in respect to the NAP during the transient phase, point towards the slow-slip event as origin. The long wavelength of observed geodetic transient confirms that the transient originates on a larger scale than localised faulting during the 2019-2020 sequence and hence most likely originates on the subducting CP interface.

The subducting oceanic crust is known to be fluid saturated (Song et al., 2009). If the fluids are released, which happens as a response to the perturbations like slow slip events (Audet et al., 2009), they would migrate from the subducting oceanic crust and drain through permeable fluid conduits (e.g. Fesola et al., 2019) like Punta Montalva or Investigator fault, raising pore pressures and lowering the effective stresses on them, thus generating seismicity (Liu et al., 2007, Colella et al., 2017). This behaviour could explain the presence of the low magnitude Caja swarm prior to the main sequence and the swarm-like behaviour of the main sequence. Drainage would in turn control the downdip extent of the seismogenic zone of the megathrust. The drier conditions of the subducting interface trenchward would promote fast seismogenic rupture while downdip the strike slip faults, fluid saturation would result in slow slip events within the transition zone (Husker et al., 2018). This cloud directly influence the seismic hazard of Puerto Rico in case of a megathrust earthquake on the Muertos subduction.

5. Data and Resources

- The Global Centroid Moment Tensor Project database was searched using www.globalcmt.org/CMTsearch.html.

- The repository of the Nevada Geodetic Laboratory was used to obtain the cGPS time series (http://geodesy.unr.edu)

- Dataset of the PR seismic network was accessed through the IRIS DMC archives.

The Supplementary to the manuscript includes a detailed descriptions of the methodologies used in the main paper and additional figures for better understanding of both the Supplementary Material and the manuscript. The Supplementary consists of next chapters:

- **Methods S1. Source-specific station term corrections**
- **Methods S2. Absolute, coherency relocation**
- **Methods S3. Kinematic rupture inversion**
- **Methods S4. GPS**
- **Methods S5. Template matching**

6. References

1. Audet, P., Bostock, M. G., Christensen, N. I., & Peacock, S. M. (2009). Seismic evidence for overpressured subducted oceanic crust and megathrust fault sealing. *Nature*, *457*(7225), 76-78.

2. Barzaghi, R., & Borghi, A. (2018). Theory of second order stationary random processes applied to GPS coordinate time-series. GPS Solutions, 22(3), 1–12.

3. Benford, B., DeMets, C., & Calais, E. (2012). GPS estimates of microplate motions, northern Caribbean: Evidence for a Hispaniola microplate and implications for earthquake hazard. *Geophysical Journal International*, *191*(2), 481-490.

4. Benz, H. (2017). Building a National Seismic Monitoring Center: NEIC from 2000 to the present. Seismological Research Letters, 88(2A), 265–269.

5. Beyreuther, M., Barsch, R., Krischer, L., Megies, T., Behr, Y., & Wassermann, J. (2010). ObsPy: A Python toolbox for seismology. Seismological Research Letters, 81(3), 530-533.

6. Blewitt, G., Hammond, W. C., & Kreemer, C. (2018). Harnessing the GPS data explosion for interdisciplinary science. Eos, 99(10.1029).

7. Borghi, A., Aoudia, A., Riva, R., & Barzaghi, R. (2009). GPS monitoring and earthquake prediction: A success story towards a useful integration. Tectonophysics, 465, 177–189, ISSN 0040-1951.

8. Borghi, A., Cannizzaro, L., & Vitti, A. (2012). Advanced techniques for discontinuity detection in GNSS coordinate time-series. An Italian case study. In Geodesy for planet Earth (pp. 627–634). Berlin, Heidelberg: Springer.

9. Borghi, A., Aoudia, A., Javed, F., & Barzaghi, R. (2016). Precursory slow-slip loaded the 2009 L'Aquila earthquake sequence. Geophysical Journal International, 205, 776–784.

10. Bruna, J. G., Muñoz-Martín, A., Ten Brink, U. S., Carbó-Gorosabel, A., Estrada, P. L., Martín-Dávila, J., ... & Morollón, M. C. (2010). Gravity modeling of the Muertos Trough and tectonic implications (north-eastern Caribbean). *Marine Geophysical Researches*, *31*(4), 263-283.

11. Bruna, J. G., Ten Brink, U. S., Muñoz-Martín, A., Carbó-Gorosabel, A., & Estrada, P. L. (2015). Shallower structure and geomorphology of the southern Puerto Rico offshore margin. *Marine and Petroleum Geology*, *67*, 30-56.

12. Chamberlain, C. J., Hopp, C. J., Boese, C. M., Warren-Smith, E., Chambers, D., Chu, S. X., ... & Townend, J. (2018). EQcorrscan: Repeating and near-repeating earthquake detection and analysis in python. Seismological Research Letters, 89(1), 173-181.

13. Colella, H. V., Sit, S. M., Brudzinski, M. R., Graham, S. E., DeMets, C., Holtkamp, S. G., ... & Arciniega-Ceballos, A. (2017). Seismicity rate increases associated with slow slip episodes prior to the 2012 Mw 7.4 Ometepec earthquake. *Earth and Planetary Science Letters*, *464*, 35-45.

14. De Barros, L., Cappa, F., Deschamps, A., & Dublanchet, P. Imbricated Aseismic Slip And Fluid Diffusion Drive A Seismic Swarm In The Corinth Gulf, Greece. *Geophysical Research Letters*.

15. DeMets, C., Gordon, R. G., & Argus, D. F. (2010). Geologically current plate motions. *Geophysical Journal International*, *181*(1), 1-80.

16. Dong, D., Fang, P., Bock, Y., Webb, F., Prawirodirdjo, L., Kedar, S., & Jamason, P. (2006). Spatiotemporal filtering using principal com- ponent analysis and Karhunen-Loeve expansion approaches for regional GPS network analysis. Journal of Geophysical Research, 111, B03405.

17. Doser, D., Rodríguez, C., & Flores, C. (2005). Historical earthquakes of the Puerto Rico-Virgin Isalnd region. *Active tectonic and seismic hazards of Puerto Rico, the Virgin Islands, and offshore areas. Mann, P.(Ed.)*, 103-114.

18. Dziewonski, A. M., Chou, T. A., & Woodhouse, J. H. (1981). Determination of earthquake source parameters from waveform data for studies of global and regional seismicity. Journal of Geophysical Research: Solid Earth, 86(B4), 2825-2852.

19. Fasola, S. L., Brudzinski, M. R., Holtkamp, S. G., Graham, S. E., & Cabral-Cano, E. (2019). Earthquake swarms and slow slip on a sliver fault in the Mexican subduction zone. Proceedings of the National Academy of Sciences, 116(15), 7198-7206.

20. Font, Y., Kao, H., Lallemand, S., Liu, C. S., & Chiao, L. Y. (2004). Hypocentre determination offshore of eastern Taiwan using the Maximum Intersection method. Geophysical Journal International, 158(2), 655-675.

21. Geller, R. J., & Mueller, C. S. (1980). Four similar earthquakes in central California. Geophysical Research Letters, 7(10), 821-824.

22. Gibbons, S. J., & Ringdal, F. (2006). The detection of low magnitude seismic events using array-based waveform correlation. Geophysical Journal International, 165(1), 149–166.

23. Gualandi, A., Serpelloni, E., & Belardinelli, M. E. (2016). Blind source separation problem in GPS time series. Journal of Geodesy, 90(4), 323–341.

24. Haynie, K. L., & Jadamec, M. A. (2017). Tectonic drivers of the Wrangell block: Insights on fore-arc sliver processes from 3-D geodynamic models of Alaska. *Tectonics*, *36*(7), 1180-1206.

25. Huérfano, V., & Bataille, K. (1994). Crustal structure and stress regime near Puerto Rico. *Seismic Bulletin: Preliminary locations of earthquakes recorded near Puerto Rico*, 15-19.

26. Huérfano, V., von Hillebrandt-Andrade, C., & Báez-Sanchez, G. (2005). Microseismic activity reveals two stress regimes in southwestern Puerto Rico. *Active Tectonics and Seismic Hazards of Puerto Rico, the Virgin Islands, and Offshore Areas*, *385*, 81-101.

27. Huérfano, V. A., Lopez, A. M., Castillo, L., Baez-Sanchez, G., Soto-Cordero, L., Lin, G., & Zhang, Q. (2010). Improving three dimensional velocity model for Puerto Rico-Virgin Islands for rapid earthquake re-locations. AGUFM, 2010, S21B-2031.

28. Husker, A., Ferrari, L., Arango-Galván, C., Corbo-Camargo, F., & Arzate-Flores, J. A. (2018). A geologic recipe for transient slip within the seismogenic zone: Insight from the Guerrero seismic gap, Mexico. Geology, 46(1), 35-38.

29. Jansma, P. E., Mattioli, G. S., Lopez, A., DeMets, C., Dixon, T. H., Mann, P., & Calais, E. (2000). Neotectonics of Puerto Rico and the Virgin Islands, northeastern Caribbean, from GPS geodesy. *Tectonics*, *19*(6), 1021-1037.

30. Jansma, P.E., Mattioli, G.S., 2005. GPS results from Puerto Rico and the Virgin Islands: constraints on tectonic setting and rates of active faulting. In: Mann, P. (Ed.), Active Tectonics and Seismic Hazards of Puerto Rico, the Virgin Islands, and Offshore Areas. Geological Society of America, pp. 13e30. Special Paper 385.

31. Ji, K. H., & Herring, T. A. (2013). A method for detecting transient signals in GPS position time-series: smoothing and principal component analysis. *Geophysical Journal International*, *193*(1), 171-186.

32. Krischer, L., Megies, T., Barsch, R., Beyreuther, M., Lecocq, T., Caudron, C., & Wassermann, J. (2015). ObsPy: A bridge for seismology into the scientific Python ecosystem. Computational Science & Discovery, 8(1), 014003.

33. Liu, B., Dai, W., Peng, W., & Meng, X. (2015). Spatiotemporal analysis of GPS time series in vertical direction using independent component analysis. Earth, Planets and Space, 67(1), 1-10.

34. Lomax, A., Virieux, J., Volant, P., & Berge-Thierry, C. (2000). Probabilistic earthquake location in 3D and layered models. In Advances in seismic event location (pp. 101-134). Springer, Dordrecht.

35. Lomax, A., Zollo, A., Capuano, P., & Virieux, J. (2001). Precise, absolute earthquake location under Somma–Vesuvius volcano using a new three-dimensional velocity model. Geophysical Journal International, 146(2), 313-331.

36. Lomax, A. (2005). A reanalysis of the hypocentral location and related observations for the great 1906 California earthquake. Bulletin of the Seismological Society of America, 95(3), 861-877.

37. Lomax, A. (2008). Location of the Focus and Tectonics of the Focal Region of the California Earthquake of 18 April 1906Location of the Focus and Tectonics of the

Focal Region of the Calif. Earthquake of 18 April 1906. Bulletin of the Seismological Society of America, 98(2), 846-860.

38. Lomax, A., Michelini, A., & Curtis, A. (2009). Earthquake location, direct, global-search methods. Encyclopedia of complexity and systems science, 5, 2449-2473.

39. Lomax, A. (2020). The 2020 Mw 6.5 Monte Cristo Range, Nevada earthquake: relocated seismicity shows rupture of a complete shear-crack system.

40. López A. M., Vanacore E., Hughes K. S., Báez-Sánchez G., and Hudgins T.R. (2020), Response and initial scientific findings from the southwestern Puerto Rico 2020 Seismic Sequence, Temblor

41. Peng, Z., & Zhao, P. (2009). Migration of early aftershocks following the 2004 Parkfield earthquake. *Nature Geoscience*, *2*(12), 877-881.

42. Piety, L. A., Redwine, J. R., Derouin, S. A., Prentice, C. S., Kelson, K. I., Klinger, R. E., & Mahan, S. (2018). Holocene Surface Ruptures on the Salinas Fault and Southeastern Great Southern Puerto Rico Fault Zone, South Coastal Plain of Puerto RicoHolocene Surface Ruptures on the Salinas Fault and Southeastern GSPRFZ, South Coastal Plain of Puerto Rico. *Bulletin of the Seismological Society of America*, *108*(2), 619-638.

43. Podvin, P., & Lecomte, I. (1991). Finite difference computation of traveltimes in very contrasted velocity models: a massively parallel approach and its associated tools. Geophysical Journal International, 105(1), 271-284.

44. Poupinet, G., Glangeaud, F., & Cote, P. (1982, May). P-time delay measurement of a doublet of microearthquakes. In ICASSP'82. IEEE International Conference on Acoustics, Speech, and Signal Processing (Vol. 7, pp. 1516-1519). IEEE.

45. Poupinet, G., Ellsworth, W. L., & Frechet, J. (1984). Monitoring velocity variations in the crust using earthquake doublets: An application to the Calaveras Fault, California. Journal of Geophysical Research: Solid Earth, 89(B7), 5719-5731.

46. Prentice, C. S., & Mann, P. (2005). Paleoseismic study of the South Lajas fault: First documentation of an onshore Holocene fault in Puerto Rico. *Active tectonics and seismic hazards of Puerto Rico, the Virgin Islands, and offshore areas: Geological Society of America Special Paper*, *385*, 215-222.

47. Reid, H. F., & Taber, S. (1919). The Porto Rico Earthquake of 1918 with Descriptions of Earlier Earthquakes: Report of the Earthquake Investigation Commission. US Government Printing Office.

48. Richards-Dinger, K. B., & Shearer, P. M. (2000). Earthquake locations in southern California obtained using source-specific station terms. Journal of Geophysical Research: Solid Earth, 105(B5), 10939-10960.

49. Roig-Silva, C. M., Asencio, E., & Joyce, J. (2013). The Northwest Trending North Boquerón Bay-Punta Montalva Fault Zone; A Through Going Active Fault System in Southwestern Puerto Rico. *Seismological Research Letters*, *84*(3), 538-550.

50. Shelly, D. R., Beroza, G. C., & Ide, S. (2007). Non-volcanic tremor and low-frequency earthquake swarms. Nature, 446(7133), 305–307. https://doi.org/10.1038/nature05666

51. Song, T. R. A., Helmberger, D. V., Brudzinski, M. R., Clayton, R. W., Davis, P., Pérez-Campos, X., & Singh, S. K. (2009). Subducting slab ultra-slow velocity layer coincident with silent earthquakes in southern Mexico. *Science*, *324*(5926), 502-506.

52. University of Puerto Rico (1986): Puerto Rico Seismic Network & Puerto Rico Strong Motion Program. International Federation of Digital Seismograph Networks. Dataset/Seismic Network. 10.7914/SN/PR

53. van Benthem, S., Govers, R., Spakman, W., & Wortel, R. (2013). Tectonic evolution and mantle structure of the Caribbean. *Journal of Geophysical Research: Solid Earth*, *118*(6), 3019-3036.

54. Vičič, B., Aoudia, A., Javed, F., Foroutan, M., & Costa, G. (2019). Geometry and mechanics of the active fault system in western Slovenia. Geophysical Journal International, 217(3), 1755-1766.

55. Vičič, B., Aoudia, A., Borghi, A., Momeni, S., & Vuan, A. (2020). Seismicity rate changes and geodetic transients in Central Apennines. Geophysical Research Letters, 47(22), e2020GL090668.

56. Vuan, A., Sugan, M., Amati, G., & Kato, A. (2018). Improving the Detection of Low-Magnitude Seismicity Preceding the Mw 6.3 L'Aquila Earthquake: Development of a Scalable Code Based on the Cross Correlation of Template. *Bulletin of the Seismological Society of America*, *108*(1), 471-480.

57. Waldhauser, Felix, and William L. Ellsworth. "A double-difference earthquake location algorithm: Method and application to the northern Hayward fault, California." *Bulletin of the Seismological Society of America* 90.6 (2000): 1353-1368.

58. Wdowinski, S., Bock, Y., Zhang, J., Fang, P., & Genrich, J. (1997). Southern California permanent GPS geodetic array: Spatial filtering of daily positions for estimating coseismic and postseismic displacements induced by the 1992 Landers earthquake. Journal of Geophysical Research, 102(B8), 18,057–18,070.

59. Xu, X., Keller, G. R., & Guo, X. (2016). Dip variations of the North American and North Caribbean Plates dominate the tectonic activity of Puerto Rico–Virgin Islands and adjacent areas. *Geological Journal*, *51*(6), 901-914.

60. Zhou, H. W. (1994). Rapid three-dimensional hypocentral determination using a master station method. Journal of Geophysical Research: Solid Earth, 99(B8), 15439-15455.